American Society of
Mechanical Engineers

ASME Accepted Manuscript Repository

Institutional Repository Cover Sheet

First Last

ASME Paper Title: Influence of Physical Electrodeposition Attributes on Mechano-Tribo and Wettability Characteristics of Ni-Co Enhanced Nanocoating

Authors: Aashish John, Adil Saeed, Zulfiqar Ahmad Khan

ASME Journal Title: Journal of Tribology

Volume/Issue 147(6) Date of Publication (VOR* Online) 14/02/2025

ASME Digital Collection URL: https://asmedigitalcollection.asme.org/

DOI: https://doi.org/10.1115/1.4067807

*VOR (version of record)

Influence of physical electrodeposition attributes on mechano-tribo and wettability characteristics of Ni-Co enhanced nanocoating.

Aashish John[1], Adil Saeed[1], Zulfiqar Ahmad Khan[1]*

[1]NanoCorr, Energy & Modelling (NCEM) Research Group, Bournemouth University, Talbot Campus, Poole, Dorset, UK

*zkhan@bournemouth.ac.uk

ABSTRACT

The current work presents a systematic exploration of the pulse electrodeposition process for Ni-Co nanocoating, with a focus on the impact of varying duty cycles (20% to 100%) and current density (3 A/dm^2 to 9 A/dm^2). The work is marked by incremental changes in duty cycle and current density and employs state-of-the-art characterisation techniques to analyse surface properties, mechanical strength, tribological behaviour and wettability. Ni-Co pulse electrodeposition at 20% duty cycle and 3 A/dm^2 current density dominates with desired attributes for the electronics and aerospace sectors with improved mechano-tribo and contact angle properties. These coatings exhibited superior performance across all aspects that have been studied. The nanotribological experiments were conducted using a novel approach to look into the nanoscale tribological behaviours, thus setting a pioneering effort in this field. Reduction in grain size (~57-83%) and enhancement in surface roughness (~64-65%) were the crucial factors contributing to improved mechanical and tribological properties. The nanohardness of the coating increased to 4.36 GPa for the optimum coating, compared to other coatings with varying properties. Similar improvements were recorded in nanotribological properties, with an improvement of ~30%-70% for coatings at 20% duty cycle and 3 A/dm^2. The synergetic effect of lower grain size, nano-hardness and surface roughness properties leads to an improved mechano-tribo coating. This advancement holds good potential for industrial applications where wear resistance and surface durability are critical. The optimal coating was analysed by employing X-ray photoelectron spectroscopy (XPS) for chemical compositions of coatings, which confirms the formation of nickel oxide and cobalt oxide. This chemical insight adds a valuable layer of understanding, reinforcing the coatings' potential for corrosion resistance and other chemical interactions in a wide range of operation environments.

Keywords:

Ni-Co pulse electrodeposition coating, composite, nano-crystalline alloys, roughness, nanotribology, contact angle.

Introduction

Since the discovery of gold coating on silver by Italian scientist Luigi V Brugnatelli in 1805 and the groundbreaking work by Michael Faraday in 1833 which laid the foundation for electrodeposition coating, the field of coating has progressed rapidly. Furthermore, introducing pulse current into the coating led to the development of pulse electrodeposition coating by L.C. Coggeshall in 1914, resulting in a smooth and uniform coating. Over the years, Ni electrodeposition has evolved with metallurgists and mechanical engineers refining and adopting pulse electrodeposition as a coating technique for various applications (which are not limited to electronics, aerospace and automobile industries), where the coatings provided enhanced mechanical, tribological and corrosive properties [1–7]. Along with these applications, pulse electrodeposition coatings tend to be quick, low-cost, porous-free, have a high deposition rate and overcome shape limitation [5,8–10].

Metallurgists and mechanical engineers are increasingly using nickel-based coatings for new coatings due to their enhanced mechanical, thermal, tribological, and magnetic properties. Ni-Co nanocrystalline coating is under constant evaluation as a replacement for the environmental problems caused by Ni-Mo coating [11,12]. Superior mechanical, thermal, magnetic, and anti-corrosive properties of Ni-Co nanocrystalline coating over pure Ni and pure Co coating have led to its use in aerospace, electronics, automotive and magnetic devices [13–15].

The parameters for pulse electrodeposition can be divided broadly into two parts: physical and chemical. The coating's physical parameters vary externally, including duty cycle, current density, frequency, deposition time, and pulse direction [16,17]. The chemical parameters are various electrolyte conditions: temperature of the electrolyte, electrolytic composition and pH of the electrolyte [17,18]. The modifications made to these chemical and physical characteristics enhance the coating quality. For instance, Ni-TiO_2 nanocomposite coating was conducted by Lajevardi et al. [19] with variations in duty cycle, current density and frequency. It was reported that intensifying current density beyond 4 A/dm^2 decreases microhardness. Similarly, a change in pulse frequency between 0.1 - 10 Hz resulted in an improved property, but further increase causes a drop in properties. Ni-Co/SiC were coated with variation in duty cycle and frequency by Chunyang et al. [20] with surface, mechanical and corrosive properties being analysed. A reduction in duty cycle correlated with a drop in grain size of 20%, exhibiting a homogeneous and smooth microstructure. A significant improvement in wear and anti-corrosive properties were observed at a lower duty cycle. The increased embedment of SiC particles at lower duty cycles resulted in decreased grain size leading to improved mechanical and tribological properties. Ziming et al [21] performed Ni-graphene pulse electrodeposition coating under varying duty cycles with supercritical carbon dioxide. It was established that coatings with a duty cycle of 25% had superior hardness and tribological properties. A decrease in microhardness occurs with shallow duty cycles which are primarily attributed to crystal distortion, dendritic crystals, and the formation of pores along grain boundaries, resulting in uneven coating. Moreover, during low-duty cycles, the OFF-time duration extends, weakening the attraction force between the substrate and nanomaterials surrounded by a cloud of positively charged metal ions. This diminished attraction may not sufficiently counteract hydrodynamic forces, potentially causing the dislodgment of nanomaterials from the substrate surface. Several researchers have used Ni-Co pulse electrodeposition coating, with a reinforcing metal matrix composite. SiO_2 was added as a reinforcing nanocomposite to Ni-Co nanocoating with variations in stirring rate, pH and SiO_2 concentration. The optimum stirring rate was 200 rpm and the microhardness varied when the stirring rate was changed to either side. Similarly, pH was optimum at 4.6 and microhardness decreased when pH was changed to 4 and 4.9 [22]. Ni-Co pulse electrodeposition with variation in peak current variations found that with lower current density and duty cycle, a coating with compact and smaller grain size was obtained [23]. Ni-Co/Al_2O_3 nanocomposite coating with variations in pulse parameters showed that pulsing during the coating process gave improved properties better than direct deposition coating [24]. Siavash et al. [25] performed electrodeposition coating with ZnO as a reinforcing nanocomposite, in which pulse deposition showed better properties. Besides these, the optimum speed of coating was reported as 300 rpm. Adhesion was the major wear mechanism observed with few abrasive layers for pulse electrodeposition coating and direct current electrodeposition coating exhibited delamination wear mechanisms. Zirconia [26] was added to the Ni-Co matrix with variation in frequency and it was observed that an increase in frequency resulted in a change in grain size from rough and porous to fine and compact structure. Similarly, pulsing during coating was seen to reduce the porosity of the coating.

Although Ni-Co has been investigated with reinforcing metal matrix composites, it has not been investigated to obtain an optimum pulse electrodeposition parameter. The current research focuses on varying duty cycles and current densities to obtain an optimum Ni-Co coating with a pulse electrodeposition technique. The tribological properties of metal matrix nanocomposite coating are subjected to scrutiny. The surface properties are analysed with a non-contact optical profilometer, scanning electron microscope (SEM) and energy dispersive spectroscopy (EDS). The mechano-tribo attributes along with contact angle were analysed with nano hardness, ball-on-plate tribometer and state-of-the-art contact angle goniometer.

Experimental Procedure

In the current study, Ni-Co composite coating was performed with the help of pulse electrodeposition coating. The cathode and anode for coating were EN1A and nickel plate, respectively. EN1A was selected as the substrate for coating due to its advantage over other materials in adhesive properties, availability and cost. A circular-shaped cathode was fabricated with a 30 mm diameter and thickness of 3.5 mm. The roughness of the cathode was made below 0.05 µm using 220, 400, 800, and 1200 grit papers. The low roughness will help in improving coating adhesion. Subsequently, substates were ultrasonicated in acetone to remove any surface contaminants present.

Table 1. Chemical composition of electrolyte used for coating.

A modified Watts solution shown in Table 1 was used as an electrolyte. Nickel sulphate and nickel chloride provide Ni to the coating along with cobalt sulphate being the main source for Co. Boric acid is used as the buffering agent. Chemicals were in crystal form with 98% purity. The electrolyte was additionally subjected to 1 hour of 10 kHz ultrasonic agitation after being magnetically stirred for 24 hours. Magnetic agitation and ultrasonic stirring ensured appropriate particle mixing and dispersion in the solution. In the last step, the pulse coating electrolyte temperature was raised and sustained at 60 °C.

A pulse power generator was used for electrodeposition coating. During duty cycle variation, a 20% increase step was made to the duty cycle, taking it from 20% to 100%. With a set frequency of 10 kHz and 3 A/dm^2 current density remained unchanged along with pH kept constant at 4.2 ± 0.2. At an electrolyte temperature of 60 °C, pulse electrodeposition was conducted with ongoing magnetic stirring and ultrasonic agitation. The coating procedure had a 1-hour time limit. Following the process, coatings were cleaned with acetone in an ultrasonic bath to eliminate all excess chemicals that had adhered to the surface. To assess coating repeatability, each coating was applied three times. Subsequently, coatings were conducted with a variation from 3 A/dm^2 to 9 A/dm^2 with an increment of 2 A/dm^2 in current density with the remaining parameters kept constant. The duty cycle was set as 20% with 10 kHz frequency. The duty cycle variations are represented as D1, D2, D3, D4 and D5 and current density variations as C1, C2, C3 and C4 (Supplementary Table 1).

The surface properties of coating such as microstructure and grain size were obtained with the help of an SEM and the elemental configuration was investigated with an EDS attached to the system. For analysing the surface properties, a non-contact 3D optical profilometer was employed and several metrics, such as Ra, Rq, Rt, Sa, Sq, St, as well as bearing area curve (BAC) were assessed. ImageJ, an open-source software was used for obtaining the grain size of the coating and was analysed.

Using a nanoindenter, coating hardness was measured. The study was made with a 3-faced pyramidal Berkovich indenter. The coatings were indented a total of 25 times, and outcomes were examined. A load of 50 mN was given with loading and unloading time of 10 sec and 20 sec respectively and a 10 sec dwell time. The nanohardness of coatings along with reduced modulus of elasticity, plastic work and elastic work were calculated and analysed.

The nanotribology tests were conducted with multi-scratch experiments. A single sliding scratch with 10 repetitions was given under two-body wear sliding systems. The loads applied were 100 mN, 200 mN and 300 mN. The wear scan length was set to 2000 µm with a load rate of 5 mN/s and a scan rate of 10 µm/s. The wear volume was recorded by the depth of the scar, which was obtained with a profilometer, and further calculations were made. The SEM analysis of the wear scar was analysed to understand the wear mechanisms involved.

For micro tribology testing, a modified reciprocating ball-on-plate tribometer was used. AISI52100 was used as a counter surface and a stroke length of 5 mm, a frequency of 5 Hz, a cycle count of 2000 and a standard contact load of 2 N were applied. Experiments have been repeated several times, at least three, for repeatability purposes. These repeated suits of experimental schedule were subjected to dry sliding conditions at standard temperature and pressure conditions. After each test, a profilometer was used to obtain both wear profiles in terms of volume and scar depth. SEM and EDS analytical tools were deployed for assessing surface morphology including wear scars of coated interfaces.

The static contact angle of coated surfaces was analysed with a custom-made state-of-the-art setup with a micropipette which provides a 7 µL droplet of distilled water. Three different spots were analysed for measurement of the static contact angle on each surface. Once the drop detaches the pipette, it wets the coated surface instantly, and a contact angle is formed. These steady-state analyses will help to understand the hydrophilic and hydrophobic properties of the coated surfaces.

Results and Discussions

Structural Characterisation

Fig 1 shows pulse electrodeposited Ni-Co composite coating micrographs of 3 A/dm² current density and variable duty cycle. It can be espied that the grain size of the coating has a direct relation with duty cycle. A fine grain structure was observed at the lower duty cycle, D1. With each increase in duty cycle, grain size became coarser. At D5, grains were coarsely arranged. Furthermore, a coating done at a lower duty cycle exhibited a dense compact structure. The structure was seen to loosen with an increase in the duty cycle. In addition to grain size, pores were also seen to increase with an increase in the duty cycle. Similar observations were made in earlier works [27].

Fig. 1. Microstructure of Ni-Co coating at duty cycle (a) 20% (b) 40% (c) 60% (d) 80% (e) 100 % and (f) grain size variation with changing duty cycle. The inside images represent lower magnification.

Fig 2 shows the microstructure of Ni-Co pulse electrodeposited coatings at a fixed duty cycle of 20% and varying current densities. Similar to the effect of the duty cycle, an increase in current density led to coarser grain sizes. Lower current densities, such as C1, resulted in fine-grained structures, while higher current densities, like C4, yielded coarser grains. These observations are consistent with previous studies. To determine the composition of Ni and Co in the coatings, EDS analysis was performed [28,29].

As the duty cycle was reduced, the current ON time came down. Correspondingly the OFF time went up. The longer OFF time will allow more particles to arrive at the double layer, subsequently getting attached to the substrate during the ON cycle. Therefore, a greater number of particles will be embedded on the substrate during lower duty cycles [30]. The occurrence of hydrogen evolution is a significant side reaction that occurs during pulse deposition coating processes and enhances nucleation sites. The evolution of hydrogen gas will be explored with XPS in the later sessions. The higher nucleation sites will lead to higher grain formation and decreased grain size. Thus, the synergetic effect of lower ON time and higher hydrogen gas evolution resulted in a decrease in grain size during low-duty cycles. Similarly, with an increase in current density (increase in peak current), the hydrogen evolution decreases, leading to lower grain growth points, and enlargement of the existing grains. Thus, an increase in current density causes a growth in grain size density [31].

Fig 2. Microstructure of Ni-Co coating at current density (a) 3 A/dm^2 (b) 5 A/dm^2 (c) 7 A/dm^2 (d) 9 A/dm^2 and (e) grain size variation with change in current density. The inside images represent lower magnification.

The EDS analysis of coatings with fluctuating duty cycles is shown in Figure 3a. At a lower duty cycle of D1, Cobalt content was 42.83% which increased to 56%, 58%, 59% and 62% at duty cycles of D2, D3, D4 and D5, respectively. In contrast to this, nickel content decreased from 57% at D1 and to 38% at D5. A constant decrease in nickel content was observed at 42%, 41%, and 40% at duty cycles D2, D3 and D4, respectively. This decrease in nickel will subsequently result in a decrease in the coating hardness, which will be explored in later sessions. The EDS of current density varied coatings are shown in Fig 3b. As observed earlier, even with the increase in current density, nickel composition decreased from 57% at C1 and to 45% at C4. This was through a series of decreases in nickel content with 48% at C2 and 46% at C4. Correspondingly, cobalt content increased with an increase in current density, with 42.% at C1, 51% at C2, 53% at C3 and 54% at C4.

Fig 3. EDS analysis of Ni-Co coating at (a) duty cycle variation and (b) current density variation

The process of transfer of nanoparticles from the electrolytic solution to the substrate-forming composite coating can be explained with the help of the Guglielmi model [32,33]. The Guglielmi model can be explained as a process composed of two stages, (i) adsorption weakening of particles on cathode and (ii) firm adsorption of particles by reduction, wherein the deposition materializes.

Roughness Characterisation

The variation of line roughness parameters Ra, Rq and Rt are shown in Fig 4**.** The line roughness of the coatings was amplified with an increase in the duty cycle. Even though all coatings were smooth (line roughness, Ra< 0.05 µm) D1 had the lowest Ra at 0.08 µm and Ra increased to 0.22 µm for D5. A small deviation in Ra was observed in D3, with a lower Ra of 0.12 µm. To get a deeper understanding, RMS roughness was analysed. Similar to Ra, Rq was also seen as increasing with increments in the duty cycle. Similarly, the total height difference between the peak and valley increased steeply with the increase in duty cycle. For D1, Rt was 1.22 µm which increased to 4.53 µm for D5.

To consider the roughness of the whole surface, surface roughness properties were analysed. Surface roughness parameters have been analysed over a range of surfaces. A similar variation in surface roughness was observed as in that of line roughness. The surface roughness increased from 0.08 µm for D1 to 0.18 µm in D5. The RMS surface roughness was also analysed, and a similar trend was observed. A deviation from the trend was observed at D3 where roughness decreased to 0.17 µm from 0.18 µm for D2 and increased further to 0.27 µm for D4. In contrast to the roughness parameter, St values increased from D1 to D5 from 5.63 µm to 13.63 µm, respectively. This increase in peak-to-valley height can be on account of an increase in grain size at higher duty cycles. The highest peak and valley height of the surface (Sp and Sv) were also analysed. A trend like that of Sa and Sq was observed for Sp. For Sp, a decline was observed at D3 with 9.02 µm. From D1 to D5, (apart from D3) an increase in height was observed, from 5.39 µm (at D1) to 16.00 µm (at D5). In contrast to these, valley height was seen to increase till D3 and was then seen to decrease. The valley was 2.88 µm for D1, increased to 4.81 µm for D3, and decreased to 3.31 µm for D5. The effects of surface roughness properties influenced the tribological and wettability properties of the coating surfaces, which were analysed.

Fig 4. Areal and Surface roughness parameters of Ni-Co coating with varying duty cycles

Similarly, the roughness parameters of current density-varied coatings were analysed and are presented in Fig 5. Similar to the duty cycle conditions, the line roughness in current density coatings also increased with an increase in the parameter. The line roughness increased from 0.08 µm for C1 to 0.25 µm for C5. The increase in line roughness was incremental with an increase in current density. The RMS line roughness was also seen to have a similar trend with increasing roughness from 0.11 µm to 0.38 µm for C1 and C5, respectively. Analogous to the duty cycle features, the total height difference between the peak and valley also increases from 1.22 µm to 4.50 µm in C1 and C5, respectively.

The surface roughness parameters for the current density varies parameters were analysed and shown in Fig 5. It was observed that the roughness increases in an incremental value from 0.08 µm to 0.15 µm from C1 to C4 and the RMS surface roughness increased from 0.12 µm to 0.34 µm for the same coatings. From these, it can be concluded that the roughness of the coatings increased with the increment in the current density parameter. Furthermore, Sp and Sq values were seen to increase similarly to that of the surface roughness. Sp exhibited an increase from 5.39 µm to 16.92 µm and the Sv decreased from 2.88 µm to 4.06 µm for C1 and C4, respectively. The change in the surface roughness parameters in the current density varied coatings can be pointed towards grain size variation observed in microstructures. The roughness parameter of current density associated coatings was due to the grain size variation observed earlier. A similar phenomenon was observed in duty cycle varied coatings [34].

Fig 5. Areal and Surface roughness parameters of Ni-Co coating with varying current densities

The bearing curve of coatings with varying duty cycles was analysed to understand the broad spectrum of peaks and valleys over the scanned surface. The number of peaks and valleys can be interpreted from the bearing area curve with MR1 and MR2 values, respectively. Fig 6 exhibits the bearing area curve of coatings with varying duty cycles. Lower duty cycle coatings showed relatively low dispersion of peaks when compared with higher duty cycle coatings. Contrary to peak values, the number of valleys increased with change in the duty cycle. Similar observations were analysed from current density coating with peaks and valleys seen to increase. These changes in peaks and valleys can have an effect over tribological and contact angle properties, which are explored in later sessions.

Fig 6. Bearing Area Curve of Ni-Co coating with (a) duty cycle and (b) current density variation

Nanohardness

Nanoindentation tests were conducted to estimate the nanomechanical properties of Ni-Co nanocomposites with different duty cycles and current densities. Nanohardness, reduced elastic modulus, plastic work, elastic work and contact depth were obtained with the Berkovick indenter and are shown in Fig 7. The indentation depth of D1 was 709 nm and nanohardness was 4.36 GPa. However, contact depth and nanohardness were changing corresponding with an increase in the duty cycle from D2 to D5. The contact depth increased through 853 nm, 899 nm, 893 nm to 926 nm for D2 to D5 and correspondingly nanohardness decreased from 4.03 GPa, 3.79 GPa, 3.54 GPa to 3.3 GPa, respectively. Along with this, plastic and elastic work were also determined. The plastic work increases with an increase in duty cycle from 10.58 nJ for D1 to 11.21 nJ, 11.54 nJ, 11.68 nJ and 10.82 nJ for D2 to D5, respectively. The increase in plastic work points towards the increased plasticity of nanocomposite coating. Similar properties were observed for elastic work which increased from 1.84 nJ to 2.03 nJ from D1 to D5.

The nanohardness of the coatings increased with increasing current density. While the nanohardness of CD1 was 4.36 GPa, it decreased to 3.19 GPa, 3.64 GPa, and 2.78 GPa for CD2, CD3, and CD4, respectively. Similarly, the reduced modulus and contact depth increased with current density, except for an anomaly at CD3. The reduced modulus decreased from 209.75 GPa for CD1 to 185.16 GPa for CD4. The contact depth increased with decreasing nanohardness from CD1 to CD4. Additionally, plastic work increased, while elastic work decreased with increasing current density from CD1 to CD4.

Fig 7. Nanohardness and Reduced Modulus of Ni-Co coating at varying (a) duty cycle and (b) current density. Plastic Work and Elastic Work of Ni-Co coating at varying (c) duty cycle and (d) current density

The hardness of the coating was influenced by grain size. As discussed earlier, a decrease in duty cycle and current density led to smaller grain sizes. With larger grain sizes, the compactness of the structure decreases, allowing for easier grain movement, which results in lower nanohardness. Conversely, smaller grain sizes hinder grain movement, leading to increased hardness. This observation aligns with previous research [35,36] Additionally, the increased concentration of ceramic particles (nickel and cobalt) in the coating may have contributed to the changes in nanohardness. [20,37,38].

The reduced modulus of elasticity showed a similar trend to nanohardness, decreasing with increasing duty cycle. Additionally, the variation in cobalt content with changes in duty cycle and current density may have influenced the nanohardness. [39]. Therefore, the synergistic effect of grain size and nickel composition resulted in increased nanohardness with decreased duty cycle and current density.

Nanotribology

The nanotribological wear of pulse electrodeposited Ni-Co coating at various duty cycles with contact loads 100 mN, 200 mN and 300 mN is shown in Fig 8a. A constant increase in wear volume was seen with an increase in duty cycle. The same trend is observed with an increase in contact load. The relationship of wear volume to duty cycle and current density are provided in Fig 8 (a) and (b). From these results, enhanced wear properties at 20% duty cycle and 3 A/dm^2 current density for coating were observed.

Fig 8. Nanowear of Ni-Co coating at 100 mN, 200 mN and 300 mN at varying (a) duty cycle and (b) current density

Archard law can be reflected in this scenario, where the wear volume of the coating surface was influenced by the effect of load and inverse effect on material hardness. The least wear resistance was observed for coating with a duty cycle of 100% and a current density of 9 A/dm^2, which has the lowest nanohardness. Furthermore, the lower grain size will allow more material contact with the counter surface. With lower grain size, less area of grains will be removed during wear testing. With an increase in grain size, the net area of material removed will increase. This can be seen with an increase in grain size and wear volume [40,41]. The initial roughness of the coating is a critical parameter in determining wear. It has been observed that coating roughness increases with higher duty cycles and current densities. An increase in roughness results in more pronounced surface peaks. During the initial stages of tribological testing, these higher peaks cause an increase in contact pressure, leading to accelerated wear. Smooth surfaces quickly reach a stable contact area, while rough surfaces take longer to do so. Consequently, initial wear cycles of rough surfaces remove more material compared to smooth surfaces, resulting in greater overall wear for rough surfaces [42,43]. The synergistic effect of hardness, grain size and surface roughness resulted in improved tribological properties at lower duty cycle and lower current density Ni-Co coatings.

Fig 9. SEM analysis of nanowear scar for duty cycle 20% and current density 3 A/dm^2 at (a) 100 mN and (b) 300 mN. SEM analysis of nanowear scar for duty cycle 100% and current density 3 A/dm^2 at (c) 100 mN and (d) 300 mN

Wear scar line roughness was analysed and correlated with wear mechanisms involved, as shown in Fig. 10. For coating D1, roughness initially decreased from 0.080 µm to 0.068 µm at a load of 100 mN. However, it then increased to 0.098 µm at 200 mN before decreasing again to 0.068 µm at 300 mN. Similar trends were observed in D2, D3, D4, and D5 coatings. Comparably, the roughness of current density coatings was also examined. For C4, line roughness was initially 0.25 µm before treatment. It then decreased to 0.086 µm at a load of 100 mN, further decreasing to 0.078 µm at 200 mN and 0.030 µm at 300 mN. These changes in roughness during nano tribo-tests are linked to the wear mechanisms involved.

During the initial tribo-cycles, the counter surface breaks the peaks of the coating. At a lower load of 100 mN, these peaks break, causing a decrease in surface roughness and resulting in a decline in line roughness. Additionally, the initial sliding alters the apparent contact area. During this phase, abrasive wear is the dominant mechanism, as confirmed by the SEM images of the wear scar (Fig. 9). Abrasion results in more scratches on the wear scar, increasing the roughness over the area and, consequently, the line roughness values. As the load increases to 200 mN and 300 mN, the wear mechanism transitions from abrasive to adhesive wear. Adhesive wear mechanisms are characterized by smoother surfaces, reflected in lower surface roughness, particularly lower than the coating roughness.

In the initial phase of tribo-testing, surface peaks serve as asperities, making primary contact with the counter surface. These peaks undergo deformation during the early cycles, subsequently engaging with the core coating surface. Coatings with lower duty cycles and current densities exhibit lower Sp values, resulting in fewer asperities and earlier interaction between the coating and counter surface during initial tribo-cycles. This reduction in peaks contributes to lower wear volume in the coating.

Fig 10. Line roughness parameter of nanowear scar at loads 100 mN, 200 mN and 300 mN at varying (a) duty cycle and (b) current density.

Coatings subjected to lower duty cycles and current densities exhibit lower surface roughness, leading to smoother surfaces. This smoother surface topography plays a crucial role in minimizing coating wear. Analysis reveals that these coatings exhibit the lowest core surface roughness, enhancing their tribological properties. The real contact area during tribo-testing primarily involves the core surface. Notably, coatings with lower duty cycles and current densities from the BAC dataset demonstrate the lowest core surface roughness, further contributing to enhanced tribological properties [44]. Additional insights into the improvement of tribological performance are provided in subsequent sections focusing on ball-on-plate tribological testing.

Tribology

Fig 11 presents the wear rate profiles of Ni-Co nanocomposite coatings at various duty cycles and current densities. As the duty cycle increased, so did the wear volume. For instance, the wear volume increased from 3.55 x 10^{15} nm^3 at D1 to 10.41 x 10^{15} nm^3 at D5, with corresponding wear rates of 0.18 x 10^{-3} mm^3/m and 0.52 x 10^{-3} mm^3/m, respectively. A similar trend was observed for varying current densities. The wear volume increased from 3.55 x 10^{15} nm^3 at C1 to 10.35 x 10^{15} nm^3 at C4, with corresponding wear rates of 0.18 x 10^{-3} mm^3/m and 0.52 x 10^{-3} mm^3/m, respectively.

Fig 11. Wear Volume of tribologically tested Ni-Co coating at varying (a) duty cycle and (b) current density

The wear rate of a material is directly proportional to applied stress and inversely proportional to the surface hardness. In the present case, the applied load is kept constant at 2 N, however, the hardness of the coating surface is seen to change. The highest hardness among the coatings was observed for 20% duty cycle and 3 A/dm^2 current density coating. This is projected over the wear rate of composite coating, wherein, coating with the highest hardness exhibits an improved wear rate. It was observed that the D1 and C1 exhibited the lowest surface roughness. Changes in the physical parameters of the coatings led to variations in roughness, specifically an increase in Sp values. This increase in Sp values results in higher contact pressure for the same loads. As contact pressure increases, the wear rate also rises, as previously explained. However, unlike the nanotribological tests which involve two-body sliding, the ball-on-plate tribological tests represent a three-body tribological interaction. During the initial sliding, the peaks of the surface are worn down, initiating three-body wear. This type of wear increases friction between the surfaces, resulting in a higher wear rate. Consequently, as the current density and duty cycle increase, the rate of three-body tribological reactions also increases, leading to an elevated wear rate. With low duty cycle and current density coating having a lower roughness and low number of peaks, the influence of three-body interaction will be reduced, leading to an improvement in tribological properties.

Fig 12 shows SEM micrographs of various coating wear profiles. When observing the wear mechanism of D1, abrasive wear was the predominant wear mechanism involved along with patches of oxide layer formation. For D2, adhesive wear was observed, along with patches of crater wear. The coating was flaked out in D2 coatings. Further increasing duty cycle, delamination was seen to increase, with D5 having a complete failure of coatings, where the coating was completely worn out. Similarly, the SEM images of tribological evaluated coating were analysed and shown in Fig 11. when moving from C1 to C4 the adhesive wear was becoming more dominant. For C2 the delamination and ploughing of coating were visible. C4 was having drastic delamination wear, similar to that of D5. Therefore, with better wear mechanisms, coating with duty cycle and current density of 20% and 3 A/dm^2 was identified as the best coating.

Fig 12. SEM of wear scar for Ni-Co coating at duty cycles (a) 20% (b) 40% (c) 60% (d) 80%, (e) 100% and current density (f) 3 A/dm^2 (g) 5 A/dm^2 (h) 7 A/dm^2 and (i) 9 A/dm^2

Wettability

The contact angle of Ni-Co composite coating with varying duty cycles was analysed. The detailed analyses of contact angle at various duty cycles are shown in Fig13a**.** All coatings exhibited a near hydrophobic condition with a contact angle of more than 80°. At a duty cycle of D1, an angle of 92.26° was observed which increased to 103.43° at a D5 duty cycle, with D2, D3 and D4 having angles of 82.30°, 94.73° and 99.17° respectively. It was observed earlier that with an increase in duty cycle, surface roughness increases. Similar observations are espied in contact angle analysis as well. Therefore, it can be connoted that roughness and contact angle have direct proportionality with each other. Earlier researchers made similar observations as well.

Fig 13. Contact angle at various Ni-Co coating (a) duty cycle variation and (b) current density variation.

Similarly, the change in contact angle with an increase in current density was analysed and is shown in Fig 13b. Identical to duty cycle coatings, with the increase in current density, the contact angle was seen to increase with current density. At a current density of C1, a water contact angle of 92.26° was observed, increasing through 92.95° at C2 and 108.10° at C3, dipping to 94.70° at C4. With increased surface roughness, the contact angle was also seen to increase, which is following the observations made in duty cycle analysis. The coating with 3 A/dm^2 and duty cycle 20% which has enhanced mechano-tribo properties exhibited a contact angle of 92.26°, which makes it a hydrophobic coating. With the hydrophobic nature of surfaces, these coatings can be used in anti-ice and anti-fog applications, along with self-cleaning applications. The hydrophobic coating will help in reducing dust retention on surfaces, which will reduce three-body interaction, reducing wear rate and increasing the life of the coating [45,46].

XPS Analysis

The surface analysis of Ni-Co pulse electrodeposited coating at a duty cycle of 20% and current density of 3 A/dm^2 was analysed with XPS and is shown in Fig 14**.** The XPS spectra of adventitious carbon, which was taken as reference are shown in Fig 14b. The XPS spectra of Ni2p and Co2p are presented in Fig 14c and Fig 14d**.**

As seen in Fig 14c**,** the deconvolution curve of Ni2p spectra can be grouped into 3 peaks. Peaks are seen at 852.12 eV, 855.79 eV and 861.39 eV. The peak at 852.12 eV (852.8 eV) can be attributed to the metallic Ni present in the coating and the peak at 855.79 eV (856.9 eV) can be characterised by NiO or $Ni(OH)_2$ species. Peak fitting at 853.98 eV (853.4 eV) can be closely associated with NiO phase. Also, the peaks at 858.32 eV and 861.39 eV can be fitted with the Ni 2p spectrum, stipulating the existence of shake-up satellite peaks [21]. The satellite peak emerges as a result of the variance between the ground state and the excited state in the process of photoelectron emission, consistently exhibiting a higher binding energy than the primary peak [47].

Fig 14. XPS spectra of Ni-Co coating at duty cycle 20% and current density 3 A/dm^2 (a) wide spectrum (b) Carbon spectrum (c) Nickel spectrum and (d) Cobalt spectrum

In addition to the reduction of Ni metal ions during the pulse electrodeposition process, the cathode goes through hydrogen evolution reaction. This can be formulated with the following.

$$2H_2O + 2e \rightarrow 2OH- + H_2 \uparrow$$

The hydrogen formed at the cathode will result in a change in pH, supposedly increasing pH value near the coating surface. The chances of the following reaction were high.

$$Ni^{2+} + 2OH \rightarrow Ni(OH)_2$$

Moreover, nickel hydroxide has the potential to release water vapour into the air and transform it into nickel oxide.

$$Ni(OH)_2 \rightarrow \quad NiO + H_2O$$

These hypotheses can be confirmed with the formation of NiO and $Ni(OH)_2$ species observed in the XPS analysis [48].

Further, the deconvolution curves of Co were extracted and analysed (Fig 14d). The peaks are observed at 777.59 eV (778.2 eV) and 780.78 eV (780.0 eV) corresponding to the metal Co and Co oxide peaks. The hydrogen gas evolved with the reaction at the cathode can result in a decrease in pH, which was mentioned earlier. Further Co can also react with hydroxide forming cobalt hydroxide, subsequently decomposing to cobalt oxide. These assumptions can be confirmed with the CoO and $Co(OH)_2$ observations in XPS analysis [49,50].

Conclusions

Ni-Co composite coatings were successfully fabricated using pulse electrodeposition at various duty cycles and current densities. The optimal conditions were identified as a 20% duty cycle and 3 A/dm² current density. These coatings were subjected to mechanical, tribological, and wettability analyses.

SEM and EDS analysis revealed that the optimal conditions yielded fine-grained structures, attributed to the synergistic effect of reduced ON time and increased hydrogen gas evolution during deposition. XPS analysis confirmed the presence of hydrogen, which played a role in grain refinement.

Enhanced nanohardness was observed for the optimal conditions, resulting from the smaller grain size and the influence of nickel during pulsed deposition.

Nanotribological and tribological tests demonstrated that the optimal coating exhibited superior wear resistance. This improvement was attributed to the synergistic effect of increased nanohardness and reduced surface roughness.

Wear scar roughness analysis indicated a decrease in line roughness as the wear mechanism transitioned from abrasive to adhesive. Abrasive wear resulted in higher surface roughness, while adhesive wear led to smoother surfaces. This study introduced a novel approach to analyse wear mechanisms using profilometry.

Contact angle measurements revealed an increase in hydrophobicity with increasing duty cycle and current density. The optimal coating exhibited a contact angle of 92.26°, indicating hydrophobic properties, making it suitable for aerospace and electronics applications.

XPS analysis confirmed the presence of nickel and cobalt oxides, hydroxides, and hydrogen on the coating surface, further supporting the role of hydrogen in grain refinement.

Acknowledgements: The authors would like to acknowledge ASMPT SMT Solutions for their financial and in-kind support (Grant No. 12285) for conducting this research. The authors extend their gratitude to Dr. Mark Isaacs from HarwellXPS for his invaluable assistance and support in the XPS characterization and analysis, provided in-kind.

References

[1] Raub, C., 1993, “The History of Electroplating,” Metal Plating and Patination, pp. 284–290. https://doi.org/10.1016/B978-0-7506-1611-9.50027-3

[2] Chitra Rubini, C., Kumaraguru, S., Kale, V. N., Rajesh, J., and Gnanamuthu, R. M., 2022, “Development of Anti-Corrosion Properties Using Ternary Electrodeposited Zn–Ni–Co Alloys from Acidic Electrolyte for Automobile Applications,” Transactions of the Institute of Metal Finishing, **100**(2), pp. 111–116. https://doi.org/10.1080/00202967.2021.2022868

[3] Pillai, A. M., Rajendra, A., and Sharma, A. K., 2012, “Pulse Electrodeposition of Nanocrystalline Nickel on AA 6061 for Space Applications,” Transactions of the Institute of Metal Finishing, **90**(1), pp. 44–51. https://doi.org/10.1179/174591911X13165161228286

[4] Wasekar, N. P., Bathini, L., Ramakrishna, L., Rao, D. S., and Padmanabham, G., 2020, “Pulsed Electrodeposition, Mechanical Properties and Wear Mechanism in Ni-W/SiC Nanocomposite Coatings Used for Automotive Applications,” Appl Surf Sci, **527**. https://doi.org/10.1016/j.apsusc.2020.146896

[5] Larson, C., and Farr, J. P. G., “Transactions of the IMF The International Journal of Surface Engineering and Coatings Current Research and Potential Applications for Pulsed Current Electrodeposition-a Review C Larson & J P G Farr* Current Research and Potential Applications for Pulsed Current Electrodeposition-a Review.” https://doi.org/10.1179/174591912X13238641755178

[6] Davim, J. P., and Charitidis, C. A., 2013, “Nanocomposites: Materials, Manufacturing and Engineering,” Nanocomposites: Materials, Manufacturing and Engineering, pp. 1–224. https://doi.org/10.1515/9783110267426

[7] Arya, R. K., Verros, G. D., and Davim, J. P., 2024, *Functional Coatings: Innovations and Challenges*, Wiley

[8] Erb, U., 1995, “Electrodeposited Nanocrystals: Synthesis, Properties and Industrial Applications,” Nanostructured Materials, **6**(5–8), pp. 533–538. https://doi.org/10.1016/0965-9773(95)00114-X

[9] Gurrappa, I., and Binder, L., 2008, “Science and Technology of Advanced Materials Electrodeposition of Nanostructured Coatings and Their Characterization-A Review Injeti Gurrappa & Leo Binder Electrodeposition of Nanostructured Coatings and Their Characterization-a Review,” Adv. Mater, **9**, pp. 43001–43012. https://doi.org/10.1088/1468-6996/9/4/043001.

[10] De Gruyter, 2017, *Progress in Green Tribology*, . https://doi.org/10.1515/9783110367058.

[11] Safavi, M. S., Tanhaei, M., Ahmadipour, M. F., Ghaffari Adli, R., Mahdavi, S., and Walsh, F. C., 2020, “Electrodeposited Ni-Co Alloy-Particle Composite Coatings: A Comprehensive Review,” Surf Coat Technol, **382**. https://doi.org/10.1016/j.surfcoat.2019.125153

[12] Karimzadeh, A., Aliofkhazraei, M., and Walsh, F. C., 2019, “A Review of Electrodeposited Ni-Co Alloy and Composite Coatings: Microstructure, Properties and Applications,” Surf Coat Technol, **372**, pp. 463–498. https://doi.org/10.1016/j.surfcoat.2019.04.079

[13] Tian, L., Xu, J., and Xiao, S., 2011, “The Influence of PH and Bath Composition on the Properties of Ni–Co Coatings Synthesized by Electrodeposition,” Vacuum, **86**(1), pp. 27–33. https://doi.org/10.1016/J.VACUUM.2011.03.027

[14] Chang, Y. J., Ho, C. Y., and Chang, C. H., 2014, “Influence of Material Properties upon Immobilization of Histidine-Tagged Protein on Ni–Co Coated Chip,” Materials Science and Engineering: C, **37**(1), pp. 369–373. https://doi.org/10.1016/J.MSEC.2014.01.028

[15] Kim, J. Y., Lee, J., and Cho, Y.-H., 2009, “Anti-Buckling S-Shaped Vertical Microprobes with Branch Springs,” Microelectron Eng, **87**, pp. 1769–1776. https://doi.org/10.1016/j.mee.2009.10.014

[16] Vazquez-Arenas, J., Altamirano-Garcia, L., Treeratanaphitak, T., Pritzker, M., Luna-Sánchez, R., and Cabrera-Sierra, R., 2012, "Electrochimica Acta Co-Ni Alloy Electrodeposition under Different Conditions of PH, Current and Composition," Electrochim Acta, **65**, pp. 234–243. https://doi.org/10.1016/j.electacta.2012.01.050

[17] Hansal, W. E. G., Tury, B., Halmdienst, M., Lakatos Varsányi, M., and Kautek, W., 2006, "Pulse Reverse Plating of Ni-Co Alloys: Deposition Kinetics of Watts, Sulfamate and Chloride Electrolytes," Electrochim Acta, **52**, pp. 1145–1151. https://doi.org/10.1016/j.electacta.2006.07.012

[18] Bai, A., and Hu, C. C., 2002, "Effects of Electroplating Variables on the Composition and Morphology of Nickel–Cobalt Deposits Plated through Means of Cyclic Voltammetry," Electrochim Acta, **47**(21), pp. 3447–3456. https://doi.org/10.1016/S0013-4686(02)00281-5

[19] Lajevardi, S. A., and Shahrabi, T., 2010, "Effects of Pulse Electrodeposition Parameters on the Properties of Ni-TiO 2 Nanocomposite Coatings," Appl Surf Sci, **256**(22), pp. 6775–6781. https://doi.org/10.1016/j.apsusc.2010.04.088

[20] Ma, C., Zhao, D., and Ma, Z., 2020, "Effects of Duty Cycle and Pulse Frequency on Microstructures and Properties of Electrodeposited Ni–Co–SiC Nanocoatings," Ceram Int, **46**(8), pp. 12128–12137. https://doi.org/10.1016/j.ceramint.2020.01.258

[21] Xue, Z., Lei, W., Wang, Y., Qian, H., and Li, Q., 2017, "Effect of Pulse Duty Cycle on Mechanical Properties and Microstructure of Nickel-Graphene Composite Coating Produced by Pulse Electrodeposition under Supercritical Carbon Dioxide," Surf Coat Technol, **325**, pp. 417–428. https://doi.org/10.1016/j.surfcoat.2017.07.017

[22] Ghazanlou, S. I., Ahmadiyeh, S., and Yavari, R., 2017, "Investigation of Pulse Electrodeposited Ni–Co/SiO2 Nanocomposite Coating," Surface Engineering, **33**(5), pp. 337–347. https://doi.org/10.1080/02670844.2016.1275484

[23] Tury, B., Lakatos-Varsányi, M., and Roy, S., 2006, “Ni–Co Alloys Plated by Pulse Currents,” Surf Coat Technol, **200**(24), pp. 6713–6717. https://doi.org/10.1016/J.SURFCOAT.2005.10.008

[24] Chang, L. M., Guo, H. F., and An, M. Z., 2008, “Electrodeposition of Ni–Co/Al2O3 Composite Coating by Pulse Reverse Method under Ultrasonic Condition,” Mater Lett, **62**(19), pp. 3313–3315. https://doi.org/10.1177/0954405419875353

[25] Imanian Ghazanlou, S., Farhood, A. H. S., Ahmadiyeh, S., Ziyaei, E., Rasooli, A., and Hosseinpour, S., 2019, “Characterization of Pulse and Direct Current Methods for Electrodeposition of Ni-Co Composite Coatings Reinforced with Nano and Micro ZnO Particles,” Metall Mater Trans A Phys Metall Mater Sci, **50**(4), pp. 1922–1935. https://doi.org/10.1007/s11661-019-05118-y

[26] Jiang, Y., Xu, Y., Wang, M., and Yao, H., 2017, “Effects of Pulse Plating Parameters on the Microstructure and Properties of High Frequency Pulse Electrodeposited Ni–Co/ZrO2 Nanocomposite Coatings,” Journal of Materials Science: Materials in Electronics, **28**(1), pp. 610–616. https://doi.org/10.1007/S10854-016-5565-3

[27] Yang, Y., and Cheng, Y. F., 2013, “Fabrication of Ni-Co-SiC Composite Coatings by Pulse Electrodeposition - Effects of Duty Cycle and Pulse Frequency,” Surf Coat Technol, **216**, pp. 282–288. https://doi.org/10.1016/j.surfcoat.2012.11.059

[28] Bakhit, B., Akbari, A., Nasirpouri, F., and Hosseini, M. G., 2014, “Corrosion Resistance of Ni-Co Alloy and Ni-Co/SiC Nanocomposite Coatings Electrodeposited by Sediment Codeposition Technique,” Appl Surf Sci, **307**, pp. 351–359. https://doi.org/10.1016/j.apsusc.2014.04.037

[29] Dheeraj, P. R., Patra, A., Sengupta, S., Das, S., and Das, K., 2017, “Synergistic Effect of Peak Current Density and Nature of Surfactant on Microstructure, Mechanical and Electrochemical Properties of Pulsed Electrodeposited Ni-Co-SiC Nanocomposites,” J Alloys Compd, **729**, pp. 1093–1107. https://doi.org/10.1016/j.jallcom.2017.09.035

[30] Lajevardi, S. A., and Shahrabi, T., 2010, “Effects of Pulse Electrodeposition Parameters on the Properties of Ni-TiO 2 Nanocomposite Coatings,” Appl Surf Sci, **256**, pp. 6775–6781. https://doi.org/10.1016/j.apsusc.2010.04.088

[31] Kim, D. J., Roh, Y. M., Seo, H., and Kim, J. S., 2004, “Effects of the Peak Current Density and Duty Cycle on Material Properties of Pulse-Plated Ni-P-Fe Electrodeposits.” https://doi.org/10.1016/j.surfcoat.2004.03.055

[32] Guglielmi, N., 1972, “Kinetics of the Deposition of Inert Particles from Electrolytic Baths,” J Electrochem Soc, **119**(8), p. 1009. https://doi.org/10.1149/1.2404383

[33] Celis, J. P., Roos, J. R., and Buelens, C., 1987, “A Mathematical Model for the Electrolytic Codeposition of Particles with a Metallic Matrix,” J Electrochem Soc, **134**(6), pp. 1402–1408. https://doi.org/10.1149/1.2100680

[34] John, A., Saeed, A., and Khan, Z. A., 2023, “Influence of the Duty Cycle of Pulse Electrodeposition-Coated Ni-Al2O3 Nanocomposites on Surface Roughness Properties,” Materials, **16**(6). https://doi.org/10.3390/ma16062192

[35] Yang, B., and Vehoff, H., 2007, “Dependence of Nanohardness upon Indentation Size and Grain Size - A Local Examination of the Interaction between Dislocations and Grain Boundaries,” Acta Mater, **55**(3), pp. 849–856. https://doi.org/10.1016/j.actamat.2006.09.004

[36] Xia, F., Li, C., Ma, C., Li, Q., and Xing, H., 2021, “Effect of Pulse Current Density on Microstructure and Wear Property of Ni-TiN Nanocoatings Deposited via Pulse Electrodeposition,” Appl Surf Sci, **538**. https://doi.org/10.1016/j.apsusc.2020.148139

[37] Xia, F., Li, Q., Ma, C., and Guo, X., 2020, “Preparation and Characterization of Ni–AlN Nanocoatings Deposited by Magnetic Field Assisted Electrodeposition Technique,” Ceram Int, **46**(2), pp. 2500–2509. https://doi.org/10.1016/j.ceramint.2019.09.244

[38] Kasar, A. K., Bhutta, M. U., Khan, Z. A., and Menezes, P. L., 2020, “Corrosion Performance of Nanocomposite Coatings in Moist SO2 Environment,” International Journal of Advanced

Manufacturing Technology, **106**(11–12), pp. 4769–4776. https://doi.org/10.1007/s00170-020-04949-z

[39] Su, F., Liu, C., and Huang, P., 2013, “Establishing Relationships between Electrodeposition Techniques, Microstructure and Properties of Nanocrystalline Co-W Alloy Coatings,” J Alloys Compd, **557**, pp. 228–238. https://doi.org/10.1016/j.jallcom.2013.01.003

[40] Xia, F., Li, C., Ma, C., Li, Q., and Xing, H., 2021, “Effect of Pulse Current Density on Microstructure and Wear Property of Ni-TiN Nanocoatings Deposited via Pulse Electrodeposition,” Appl Surf Sci, **538**. https://doi.org/10.1016/j.apsusc.2020.148139

[41] John, A., Showket, J., Joseph Babu, K., Edachery, V., and Suvin, P. S., 2023, “Micro-Tribological Characteristics of Ti6Al4V Alloy Subjected to Shot Blasting Surface Treatment Process,” Transactions of the Indian Institute of Metals, **76**(9), pp. 2463–2471. https://doi.org/10.1007/s12666-023-02915-3

[42] Pawlus, P., Michalczewski, R., Lenart, A., and Dzierwa, A., 2014, “The Effect of Random Surface Topography Height on Fretting in Dry Gross Slip Conditions,” Proceedings of the Institution of Mechanical Engineers, Part J: Journal of Engineering Tribology, **228**(12), pp. 1374–1391. https://doi.org/10.1177/1350650114539467

[43] Lehtovaara A, Lönnqvist C. “Modelling and analysis of fretting wear in rough point contacts in partial slip conditions”. Proceedings of the Institution of Mechanical Engineers, Part J: Journal of Engineering Tribology. 2011;225(10):986-998. doi:10.1177/1350650111417215

[44] J.P. Davim (ed.), Tribology for Engineers | Elsevier, ScienceDirect, (n.d.). https://www.sciencedirect.com/book/9780857091147/tribology-for-engineers

[45] Horng, J. H., Yu, C. C., and Chen, Y. Y., 2022, “Tribological Characteristics and Load-Sharing of Point-Contact Interface in Three-Body Mixed Lubrication,” J Tribol, **144**(5). https://doi.org/10.1115/1.4052964

[46] Sardar, S., Karmakar, S. K., and Das, D., 2018, “Tribological Properties of Al 7075 Alloy and 7075/Al 2 O 3 Composite under Two-Body Abrasion: A Statistical Approach,” J Tribol, **140**(5). https://doi.org/10.1115/1.4039410

[47] Do, Q., An, H., Wang, G., Meng, G., Wang, Y., Liu, B., Wang, J., and Wang, F., 2019, “Effect of Cupric Sulfate on the Microstructure and Corrosion Behavior of Nickel-Copper Nanostructure Coatings Synthesized by Pulsed Electrodeposition Technique,” Corros Sci, **147**, pp. 246–259. https://doi.org/10.1016/j.corsci.2018.11.017

[48] Li, B., and Zhang, W., 2018, “Microstructural, Surface and Electrochemical Properties of Pulse Electrodeposited Ni–W/Si3N4 Nanocomposite Coating,” Ceram Int, **44**(16), pp. 19907–19918. https://doi.org/10.1016/j.ceramint.2018.07.254

[49] Khorsand, S., Raeissi, K., Ashrafizadeh, F., and Arenas, M. A., 2015, “Relationship between the Structure and Water Repellency of Nickel-Cobalt Alloy Coatings Prepared by Electrodeposition Process,” Surf Coat Technol, **276**, pp. 296–304. https://doi.org/10.1016/j.surfcoat.2015.07.010

[50] Bera, P., Seenivasan, H., Rajam, K. S., and William Grips, V. K., 2012, “Characterization of Amorphous Co-P Alloy Coatings Electrodeposited with Pulse Current Using Gluconate Bath,” Appl Surf Sci, **258**(24), pp. 9544–9553. https://doi.org/10.1016/j.apsusc.2012.05.115

Supplementary Data

Supplementary Fig 1. Profilometry of Ni-Co coating at duty cycle (a) 20% (b) 40% (c) 60% (d) 80% and (e) 100 %

Supplementary Fig 2. Profilometry of Ni-Co coating at current density (a) 3 A/dm^2 (b) 5 A/dm^2 (c) 7 A/dm^2 and (d) 9 A/dm^2

Supplementary Fig 3. Wear Scar profile of Ni-Co nanocoating with duty cycle variation at (a) 100 mN, (b) 200 mN and (c) 300 mN

Supplementary Fig 4. Wear Scar profile of Ni-Co nanocoating with current density variation at (a) 100 mN, (b) 200 mN and (c) 300 mN

Supplementary Fig 5. Contact angle of Ni-Co coating at duty cycle (a) 20% (b) 40% (c) 60% (d) 80% (e) 100% and current density (b) 5 A/dm^2 (c) 7 A/dm^2 and (d) 9 A/dm^2

Supplementary Table 1. Physical parameters used for pulse electrodeposition coating of Ni-Co coating.

Conditions	
Current Density (A/dm^2)	3, 5, 7, 9
Duty Cycle (%)	20, 40, 60, 80, 100
pH	4.2 ± 0.2
Time (mins)	60
Temperature (C)	60 ± 5
Stir Speed (rpm)	300
Cathode	Mild Steel
Anode	Nickel Plate
Distance bw electrodes (mm)	40

Supplementary Table 2. Nanotribology wear volume and line roughness of duty cycle varied coatings at various loads.

Duty Cycle (%)	100 mN				200 mN				300 mN		
	Ra (µm)	Rq (µm)	Wear Volume (x10^{-3} mm^3)		Ra (µm)	Rq (µm)	Wear Volume (x10^{-3} mm^3)		Ra (µm)	Rq (µm)	Wear Volume (x10^{-3} mm^3)
20	0.069	0.082	1.911		0.098	0.110	4.520		0.068	0.084	4.968
40	0.066	0.083	4.387		0.061	0.077	5.444		0.065	0.051	6.871
60	0.048	0.061	4.761		0.070	0.092	5.516		0.047	0.059	6.355
80	0.072	0.098	5.177		0.080	0.109	5.797		0.061	0.073	6.932
100	0.059	0.074	5.907		0.048	0.062	6.512		0.051	0.063	7.244

Supplementary Table 3. Nanotribology wear volume and line roughness of current density varied coatings at various loads.

Current Density (A/dm^2)	100 mN				200 mN				300 mN		
	Ra (μm)	Rq (μm)	Wear Volume(x 10^{-3} mm^3)		Ra (μm)	Rq (μm)	Wear Volume(x 10^{-3} mm^3)		Ra (μm)	Rq (μm)	Wear Volume(x 10^{-3} mm^3)
3	0.069	0.082	1.911		0.098	0.110	4.520		0.068	0.084	4.968
5	0.049	0.061	5.263		0.037	0.044	4.867		0.046	0.054	5.297
7	0.036	0.045	5.944		0.034	0.044	5.461		0.057	0.073	6.163
9	0.087	0.113	6.243		0.078	0.093	7.883		0.031	0.040	8.272

LIST OF FIGURES

Fig. 1. Microstructure of Ni-Co coating at duty cycle (a) 20% (b) 40% (c) 60% (d) 80% (e) 100 % and (f) grain size variation with changing duty cycle. The inside images represent lower magnification.

Fig. 2. Microstructure of Ni-Co coating at current density (a) 3 A/dm^2 (b) 5 A/dm^2 (c) 7 A/dm^2 (d) 9 A/dm^2 and (e) grain size variation with change in current density. The inside images represent lower magnification.

Fig. 3. EDS analysis of Ni-Co coating at (a) duty cycle variation and (b) current density variation

Fig. 4. Areal and Surface roughness parameters of Ni-Co coating with varying duty cycles.

Fig. 5. Areal and Surface roughness parameters of Ni-Co coating with varying current densities

Fig. 6. Bearing Area Curve of Ni-Co coating with (a) duty cycle and (b) current density variation.

Fig. 7. Nanohardness and Reduced Modulus of Ni-Co coating at varying (a) duty cycle and (b) current density. Plastic Work and Elastic Work of Ni-Co coating at varying (c) duty cycle and (d) current density.

Fig. 8. Nanowear of Ni-Co coating at 100 mN, 200 mN and 300 mN at varying (a) duty cycle and (b) current density.

Fig. 9. SEM analysis of nanowear scar for duty cycle 20% and current density 3 A/dm^2 at (a) 100 mN and (b) 300 mN. SEM analysis of nanowear scar for duty cycle 100% and current density 3 A/dm^2 at (c) 100 mN and (d) 300 mN

Fig. 10. Line roughness parameter of nanowear scar at loads 100 mN, 200 mN and 300 mN at varying (a) duty cycle and (b) current density.

Fig. 11. Wear Volume of tribologically tested Ni-Co coating at varying (a) duty cycle and (b) current density.

Fig. 12. SEM of wear scar for Ni-Co coating at duty cycles (a) 20% (b) 40% (c) 60% (d) 80%, (e) 100% and current density (f) 3 A/dm^2 (g) 5 A/dm^2 (h) 7 A/dm^2 and (i) 9 A/dm^2

Fig. 13. Contact angle at various Ni-Co coating (a) duty cycle variation and (b) current density variation.

Fig. 14. XPS spectra of Ni-Co coating at duty cycle 20% and current density 3 A/dm^2 (a) wide spectrum (b) Carbon spectrum (c) Nickel spectrum and (d) Cobalt spectrum.

LIST OF SUPPLEMENTARY FIGURES

Supplementary Fig 1. Profilometry of Ni-Co coating at duty cycle (a) 20% (b) 40% (c) 60% (d) 80% and (e) 100 %

Supplementary Fig 2. Profilometry of Ni-Co coating at current density (a) 3 A/dm^2 (b) 5 A/dm^2 (c) 7 A/dm^2 and (d) 9 A/dm^2

Supplementary Fig 3. Wear Scar profile of Ni-Co nanocoating with duty cycle variation at (a) 100 mN, (b) 200 mN and (c) 300 mN

Supplementary Fig 4. Wear Scar profile of Ni-Co nanocoating with current density variation at (a) 100 mN, (b) 200 mN and (c) 300 mN

Supplementary Fig 5. Contact angle of Ni-Co coating at duty cycle (a) 20% (b) 40% (c) 60% (d) 80% (e) 100% and current density (b) 5 A/dm^2 (c) 7 A/dm^2 and (d) 9 A/dm^2

TABLES

Table 1. Chemical composition of electrolyte used for coating.

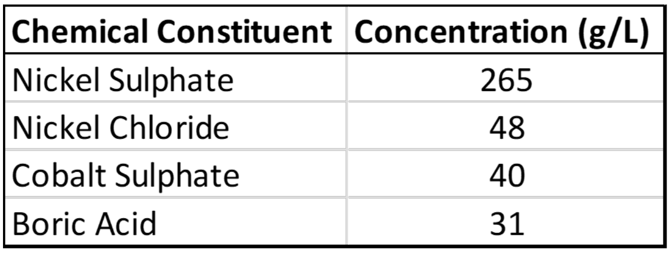

Chemical Constituent	Concentration (g/L)
Nickel Sulphate	265
Nickel Chloride	48
Cobalt Sulphate	40
Boric Acid	31